Materials Today Sustainability 30 (2025) 101099

Contents lists available at ScienceDirect

Materials Today Sustainability

journal homepage: www.journals.elsevier.com/materials-today-sustainability

Innovative multiphase composites of transition metal oxides for long-term stability and high energy density in storage devices

Nayab Zahra [a], Muhammad Shahbaz [b], Mohsin Saleem [c,**], Muhammad Zubair Khan [d,****], Muneeb Irshad [e], Shahzad Sharif [b], Jung Hyuk Koh [g,***], Mohsin Ali Marwat [f], Gwangseop Lee [g,h], Muhammad Irfan [c], Abdul Ghaffar [a,*]

[a] Department of Physics, Government College University, Lahore, 54000 Pakistan
[b] Materials Chemistry Laboratory, Institute of Chemical Sciences, Government College University Lahore, 54000, Pakistan
[c] School of Chemical and Materials Engineering (SCME), National University of Sciences and Technology (NUST), H-12, Islamabad, 44000, Pakistan
[d] Pak-Austria Fachhochschule: Institute of Applied Sciences, Department of Materials Science and Engineering, Haripur, KPK, Pakistan
[e] Department of Physics, University of Engineering and Technology, Lahore, 54890, Pakistan
[f] Faculty of Materials and Chemical Engineering, Ghulam Ishaq Khan (GIK) Institute of Engineering Sciences and Technology, Topi 23640, Pakistan
[g] School of Electrical and Electronic Engineering, Chung-Ang University, Seoul, Republic of Korea
[h] Graduate School of Intelligent Energy and Industry, Chung-Ang University, Seoul, Republic of Korea

ARTICLE INFO

Keywords:
Multiphase nanomaterial
Metal oxides
Solution combustion synthesis
Charge storage
Supercapacitor

ABSTRACT

The development of an optimal material that facilitates multiple redox reactions is crucial for advancing energy storage devices. In the present study, we focused on preparing such a material through an easy and cost-effective method to achieve enhanced charge storage ability with large power. Multiphase composites based on Mn, Ce, Co, and Ni oxides were prepared via solution combustion synthesis (SCS) for supercapacitor electrode applications. Three composites, Mn–O/CeO_2 (N1), Ni–O/Co_3O_4 (N2), and Mn–O/CeO_2/Ni–O/Co_3O_4 (N3), all in equal ratios, were prepared after sintering at 700 °C for 3 h in the open air. Preliminary characterizations, including X-ray diffraction (XRD), diffuse reflectance spectroscopy (DRS), Raman spectroscopy, and scanning electron microscopy (SEM), were performed to investigate the structural, optical, and morphological properties of the three distinct composites. XRD analysis confirmed the presence of various phases, such as CeO_2, Mn_2O_3, Co_3O_4, NiO, Ni_2O_3, and Mn_5O_8 in the different composites, significantly influencing their physical and electrochemical behavior. With three-electrode assembly, electroanalytical tools such as cyclic voltammetry (CV), galvanic charge-discharge (GCD), and electrochemical impedance spectroscopy (EIS) were utilized to divulge electrochemical properties which confirmed pseudocapacitive behavior in the synthesized electrode composites. The specific capacitance of 59.3 F/g, 91.67 F/g, and 23.14 F/g at a current density of 1 A/g were recorded for N1, N2, and N3, respectively. Having tempting results of N2 cathode, it was fabricated against activated carbon (AC) anode to form a hybrid supercapacitor device which demonstrated a specific capacitance of 78.25 F/g, a specific energy of 24.45 Wh/kg, and a large specific power of 1086.80 W/kg at 1 A/g current density, with a coulombic efficiency of 106.5% over 1000 GCD cycles.

1. Introduction

Energy generation and storage are critical concerns today due to the growing energy demands across various sectors of daily life [1]. The depletion of natural resources and associated environmental issues necessitate the development of reliable, high-performance devices that can compete with batteries [2,3], supercapacitors [4–6], and solid oxide fuel cells (SOFCs) [7,8] in terms of energy storage. The primary

* Corresponding authors.
** Corresponding author.
*** Corresponding authors.
**** Corresponding author.
E-mail addresses: mohsin852@cau.ac.kr, mohsin.saleem@scme.nust.edu.pk (M. Saleem), zubair.khan@fcm3.paf-iast.edu.pk (M.Z. Khan), jhkoh@cau.ac.kr (J.H. Koh), abdulghaffar@gcu.edu.pk (A. Ghaffar).

https://doi.org/10.1016/j.mtsust.2025.101099
Received 24 November 2024; Received in revised form 7 February 2025; Accepted 6 March 2025
Available online 8 March 2025

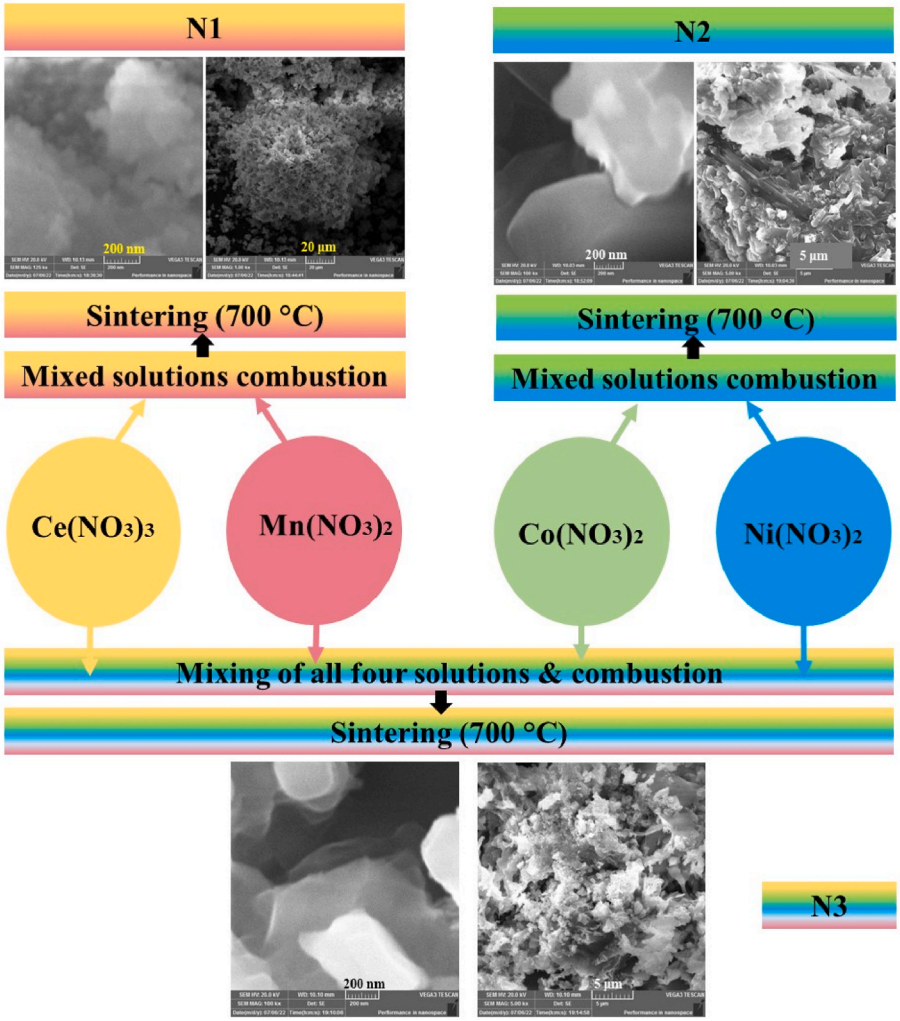

Fig. 1. Schematic illustration of the solution combustion synthesis approach adopted in the present study.

applications of energy storage devices include low-power electronics, high-power military systems, electric vehicles, and hybrid energy storage systems [9].

The self-discharge, electrical response, and thermal properties of materials have been extensively investigated through both experimental methods and theoretical modeling [10]. The interfacial interactions between the electrode material and the electrolyte predominantly govern the electrochemical properties of charge-storing devices. The underlying redox processes are significantly influenced by the electrode material used as the electrode [11]. Metal oxide nanostructures have emerged as a focal point in supercapacitor electrode research, where modification strategies are crucial for overcoming limitations such as low energy density and poor cycle life [12,13]. Various supercapacitor configurations, such as pseudo capacitors, double-layer capacitors, and hybrids, are being developed for charge storage with the primary distinction of employed materials [14,15].

Supercapacitors' efficiency mainly depends on the choice of electrode material in the form of metals or metal oxides [16]. Along with the flexible [17,18] and hybrid supercapacitor electrode materials [19,20], the metal oxide-based electrodes still reveal their new features under different synthesis conditions. Metal oxides are particularly favorite as electrodes due to their potential for ultra-high storage capacitive devices [21]. Depending upon the preparation routes, resultant nanomaterials acquire certain morphological attributes, such as surface area, porosity, particle size, and crystallite size. Additional chosen post-synthesis conditions are also critical for enhancing electrochemical activity and charge storage [22,23].

Metal oxides are well-known for their electrical conductivity, making them ideal candidates for electrode materials [24,25]. Mixed metal oxides have demonstrated superior conductivity essential for charge storage mechanisms compared to the conductivities of their constituent elements [26]. Mn–O, an environmentally friendly metal oxide, is extensively used in batteries and supercapacitor devices due to its well-established electrochemical properties. Mn_3O_4 [27], MnO_2 [28], and Mn_2O_3 [29] as the manganese oxide phases exhibited moderate to significant electrochemical performance due to morphological features acquired during synthesis and the elemental composition. CeO_2, when employed as an electrode material with different Na_2SO_4, KCl, NaCl, and K_2SO_4 electrolytes, has the optimal supercapacitive performance of 523 F/g at 2 mV/s seen in the case of NaCl [30]. CeO_2 nanoparticles uniformly coated on MnO_2 nanorods have demonstrated better charge storage properties, showcasing the combined effects of the electronic features of both metal oxides [31,32]. In another example of the MnO_2/CeO_2 composite, the pore characteristics are correlated with the electrochemical performance of the final device [33]. Among other metal oxides, Co_3O_4 is an excellent choice due to its cost-effectiveness, abundance, and promising potential in energy storage applications [34]. Similarly, Ni–O nanostructures exhibit high specific capacitance and exceptional cyclic stability, making them promising candidates for advanced supercapacitor applications [35–37]. In mixtures of metal oxides, such as $NixCo_{3-x}O_4$ (with varying divalent metals) and Ni/Co metal in an electrode configuration with a 1:1 ratio, the highest specific

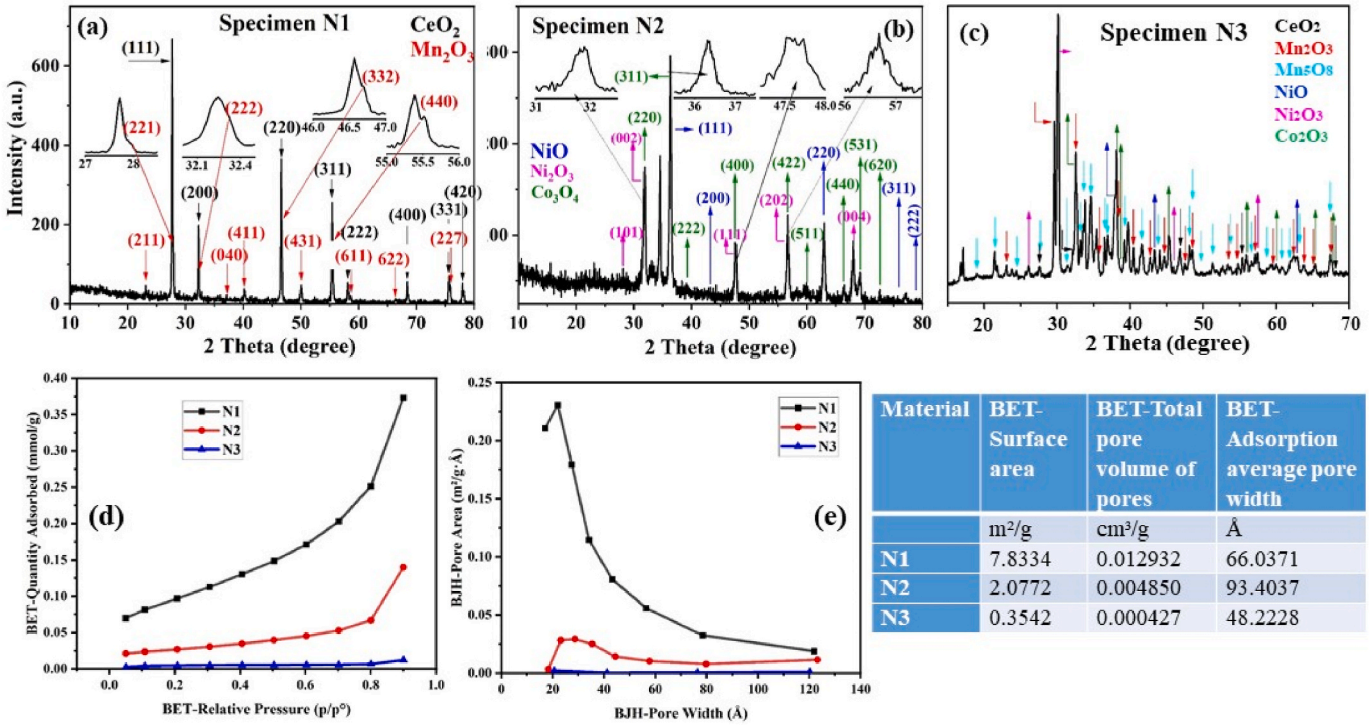

Material	BET-Surface area	BET-Total pore volume of pores	BET-Adsorption average pore width
	m^2/g	cm^3/g	Å
N1	7.8334	0.012932	66.0371
N2	2.0772	0.004850	93.4037
N3	0.3542	0.000427	48.2228

Fig. 2. XRD profiles of (a) CeO_2 and Mn_2O_3 in the form of a composite, (b) Ni–O and Co_3O_4 composite, and (c) the crystalline phases-mixture based on Ce, Mn, Ni, and Co oxides. (d) Nitrogen-adsorption isotherms of N1, N2 and N3. (e) Pore size distributions of all three samples.

capacitance (C_s) of 797 F/g with good retention has been achieved [38]. Additionally, composite materials based on Mn and Ni oxides have revealed excellent specific capacitance with good retention properties [39,40]. A composite made of NiO–Co_3O_4 with reduced graphene oxide, developed by the hydrothermal method, exhibited a specific capacity of 149 mAh/g at 0.5 A/g with good retention [41].

In the present study, four different metal oxides—Mn-O, Ce–O, Co–O, and Ni–O—are considered in different composite forms to explore their potential as electrode materials. These composite materials are synthesized via a simple, rapid, and economical solution combustion synthesis (SCS) method. As a multiphase system, multiple redox reactions are suggested within the electrode material, leading to an effective charge storage mechanism.

2. Experimental

2.1. Synthesis of materials

Reagents were purchased from Sigma-Aldrich and used to prepare the specimens in this study. The selected metal oxide-based composites were synthesized using solution combustion synthesis [42] with an exothermic redox reaction as the underlying mechanism. Among the i) high-temperature self-propagating synthesis, ii) solution combustion synthesis, and iii) gaseous phase synthesis, the solution combustion route is famous for high yield and purity [43]. The heat energy supplied triggers the necessary reaction among the metal salts used as precursors. This reaction propagates through adjacent layers, eventually leading to the ignition of the entire solution. To initiate the combustion process, a suitable fuel (such as oxalic acid, urea, or glycine) is used in an optimal ratio to achieve the required decomposition temperature, which varies based on the physicochemical properties of the selected precursors [44].

2.1.1. Specimen N1 (Mn–O: CeO_2)

To prepare, N1 (Mn–O: CeO_2) sample, $Mn(NO_3)_2{\cdot}4H_2O$ with purity ≥97% and $Ce(NO_3)_3{\cdot}6H_2O$ having purity ≥98.5% precursors were dissolved in 100 mL of deionized water (DIW) separately in a 1:1 wt%. After heating at 100 °C for a few minutes, they were mixed. To attain decomposition of the precursors in a solution, the oxalic acid as a fuel was added to the mixture solution and heated at 100 °C again. After 4 h, the DIW was desiccated and formed a gel-like material. On further heating, after ignition and burning fumes were produced and the gel-transformed to powder. Finally, the composite powder was sintered at 700 °C for 3 h in ambient conditions.

2.1.2. Specimen N2 (Co–O:Ni–O)

The precursors $Co(NO_3)_2{\cdot}6H_2O$ with purity ≥98% and $Ni(NO_3)_2{\cdot}6H_2O$ 99% pure were separately dissolved in 100 mL of DIW in a 1:1 wt% for the preparation of N2 (Co–O: Ni–O) specimen. Both solutions were heated at 100 °C for 20 min and then mixed. To achieve the decomposition temperature of the reagents, oxalic acid as a fuel was added to the mixture solution, and the temperature was set at 100 °C. After 4.5 h, the DIW evaporated, and a gel-like material was left. On further heating, the process of ignition, burning, and production took place inside the gel. Eventually, a dried powder was attained, which was later sintered at 700 °C for 3 h in the open air.

2.1.3. Specimen N3 (Mn, Ce, Co, Ni oxides)

Mn, Ce, Co, and Ni oxides (referred to as the N3 specimen) were prepared by first dissolving $Mn(NO_3)_2{\cdot}4H_2O$, $Ce(NO_3)_3{\cdot}6H_2O$, $Co(NO_3)_2{\cdot}6H_2O$, and $Ni(NO_3)_2{\cdot}6H_2O$ in 50 mL of DIW at a 1:1:1:1 wt ratio. Each solution was heated separately at 100 °C for several minutes. The solutions were then combined and further heated at 100 °C for 10 min to ensure homogenization. At this point, oxalic acid was added to the mixture to break the chemical bonds of the reagents. Keeping the solution at 100 °C for 5 hresulted in a gel-like end material. This gel was subsequently transformed into an ash-like powder upon drying. The powder was collected and subjected to a sintering process at 700 °C for 3 h under ambient conditions. The schematic of the solution combustion method is depicted in Fig. 1.

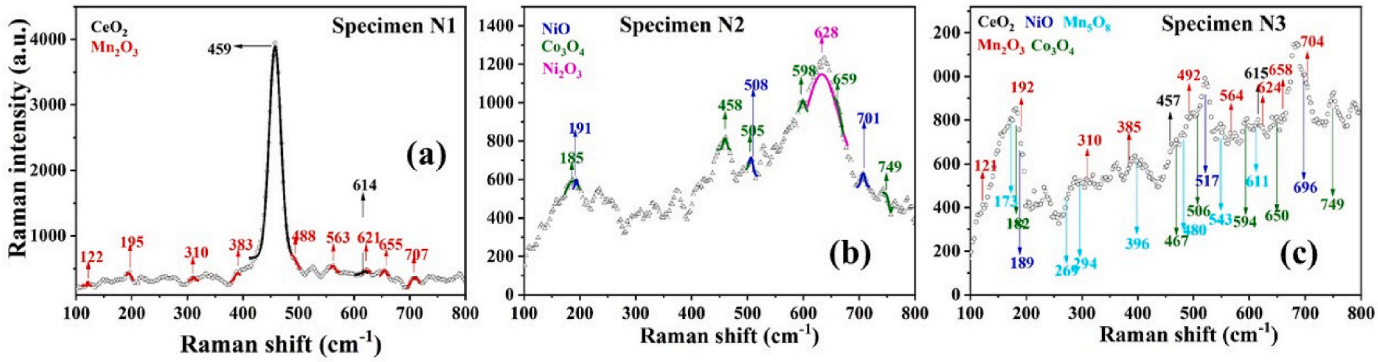

Fig. 3. Raman spectra of composite N1, N2, and N3 in the 100-800 cm^{-1} range. (a) CeO_2:Mn_2O_3 (b) Co_3O_4: NiO and (c) CeO_2, Mn_2O_3, Mn_5O_8, Co_3O_4 and NiO.

2.2. Material characterization

X-ray diffraction (XRD) measurements of the prepared powdered samples were performed using a Rigaku MiniFlex benchtop setup, employing Cu-K_α-1 X-rays with a wavelength of 0.15405 nm. Raman analysis was conducted with an i-Raman® USA system, equipped with a 532 nm laser and a resolution of ~4.5 cm^{-1} at 614 nm. The optical properties and band gaps of specimens N1, N2, and N3 were determined using a PerkinElmer Lambda 950 photo spectrometer within the wavelength range of 175–3300 nm and a resolution of 0.05 nm. Vibrational modes present in the prepared specimens were recorded using an Alpha FTIR spectrometer by Bruker, covering a wavenumber range of 4000−500 cm^{-1}. The morphology and particle distribution of the multimetal-based composites were examined using a TESCAN VEGA Scanning Electron Microscope (SEM). The composite powder was mounted on conductive carbon tape for scanning. Gemini VII 2390 by Micromeritics Instrument Corp. was utilized for the BET (Brunauer–Emmett–Teller) analysis based on nitrogen absorption.

An electrochemical analysis was conducted using an Origalys electrochemical workstation. A silver/silver chloride (Ag/AgCl) electrode served as the reference, while a platinum (Pt) electrode acted as the counter electrode. A 1 M KOH solution was used as an electrolyte. The synthesized material was deposited onto nickel foam (NF), which functioned as the working electrode. Prior to deposition, the NF was cleaned with 1 M HCl, acetone, and deionized water to remove impurities. A homogenous slurry was prepared by stirring 4 mg of the active material, 0.5 mg of polyvinylidene fluoride (PVDF) as a binder, 0.5 mg of activated carbon (AC), and 50 μL of N-methyl pyrrolidone (NMP) solvent for 6 h. The slurry was then spread onto the pre-treated NF using the drop-casting technique and dried in an oven at 60 °C for 4 h. For the two-electrode system, the AC electrode was prepared using a similar proportion of binder and solvent [45]. The amount of AC required to be deposited on the NF was calculated using equation (1) [46].

$$\frac{m_+}{m_-} = \frac{C_{s-} \times \Delta V_+}{C_{s+} \times \Delta V_-} \quad (1)$$

where m_+ and m- are masses of active materials, ΔV_+ and ΔV- are operating voltages, and C_{s+} and C_{s-} represent specific capacities (C_s). EIS was performed in the 1 MHz to 100 kHz frequency range of an AC voltage of 10 mV.

3. Results and discussion

The XRD analysis provided crucial insights into the crystalline phases present in the synthesized specimens. The XRD analysis of specimen N1 revealed the presence of CeO_2 (FCC phase) and Mn_2O_3 (BCC phase), as indexed in Fig. 2a. The Bragg peaks corresponding to Mn_2O_3 align with the JCPDS ICDD 78–0390 [47], while the diffraction peaks for CeO_2 conform to the JCPDS reference 81–0792 [48]. The identification of these phases is crucial as CeO_2 is known for its high oxygen storage capacity and redox behavior, making it valuable in catalytic applications. Mn_2O_3, on the other hand, is commonly associated with magnetic properties and is used in various electronic applications. During the sintering process, MnO_2 (JCPDS-ICDD file card# 72–1982) initially formed as the parent phase, which subsequently transformed into Mn_5O_8, an intermediate phase, before ultimately resulting in Mn_2O_3 [49]. The transformation sequence from MnO_2 to Mn_2O_3 via Mn_5O_8 is typical in manganese oxides, driven by temperature-dependent oxygen release and rearrangement of the manganese-oxygen framework, which affects the material's final magnetic and electronic properties.

For specimen N2, the XRD pattern in Fig. 2b consists of Ni–O and Co_3O_4 phases. Co_3O_4, an FCC phase, is indexed by the Bragg peaks at (220), (311), (400), (422), (511), and (440) planes, corresponding to 28.11°, 32.12°, 43.3°, 54.4°, 55.01°, and 61.9°, respectively based on JCPDS No. 74–1657 [50]. Similarly, the NiO phase in the XRD spectrum of N2 an FCC phase is defined based on JCPDS No. 04–0835 as the Bragg planes (111), (200), (220), and (222) present at 36.3°, 43.1°, 62.9°, and 75.9°, respectively [51]. NiO is widely studied for its potential in battery applications due to its high theoretical capacity and good electrical conductivity. The presence of these phases in specimen N2 suggests potential applications in energy storage and catalysis.

It is well-established in the literature that the Ni_2O_3 phase crystallizes within the temperature range of 500–700 °C, as indicated by the Ni^{3+} peak in the XPS spectrum [52]. In the current investigations, the Ni_2O_3 phase is also indexed with the (101), (002), (111), (202), and (004) planes at 23.0°, 31.7°, 47.3°, 56.5°, and 67.7°, respectively. This is a hexagonal structure and the corresponding JCPDS card no. is 14–0481. These findings provide a comprehensive understanding of the structural composition of the synthesized materials. Ni_2O_3, though less commonly studied than NiO, exhibits interesting properties, particularly in catalysis, due to its higher oxidation state and the associated ability to facilitate redox reactions. These findings provide a thorough understanding of the structural composition of the synthesized materials, which is critical for tailoring their properties for specific applications such as catalysis, energy storage, and electronic devices.

In the case of specimen N3, Mn–O, and Ni–O phases are identified along with the CeO_2 and Co_3O_4 developed during the synthesis. These are the same phases as indexed for N1 and N2 specimens. All the phases are indicated at their respective 2θ positions in Fig. 2c. Monoclinic Mn_5O_8 is readily indexed, and the respective Bragg peaks are well matched with the JCPDS card no. 39–1218 of space group *C2/m* [53].

Fig. 2d and e depict a Type III isotherm, which arises from a multilayer formation process. This behavior is attributed to the fact that the inter- and intra-metal oxide interactions in N1, N2, and N3 are stronger than their interactions with the adsorbed molecules. It is well known that a higher surface area provides more active sites for multiple redox reactions, enhancing charge storage capability. BET analysis, as presented in the table of Fig. 2, indicates that N1 possesses a larger surface area with a smaller average pore size compared to N2. However, despite

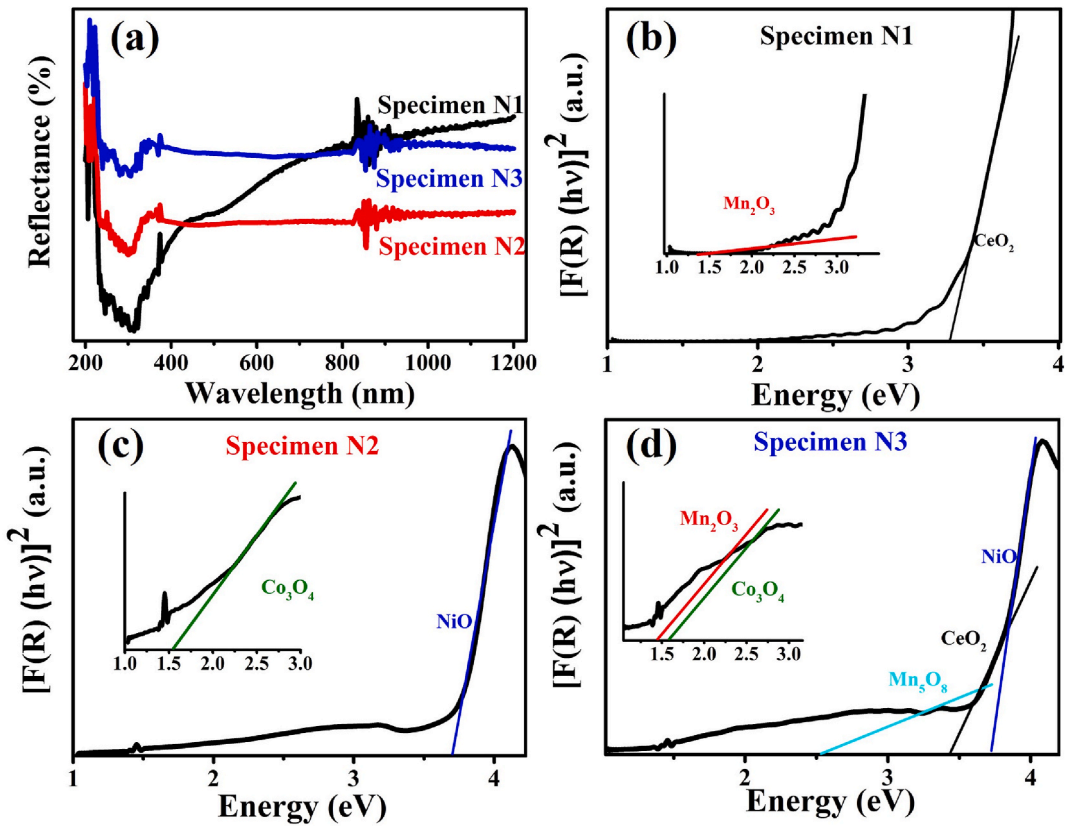

Fig. 4. (a) UV–Vis DRS spectra of all specimens. (b) Band gap energies of Mn_2O_3 and CeO_2 in a composite N1. (c) Band gap energies of Co_3O_4 and NiO composite N2. (d) Band gap energies of Mn_2O_3, CeO_2, Co_3O_4, NiO and Mn_5O_8 as multimetal oxide composite N3.

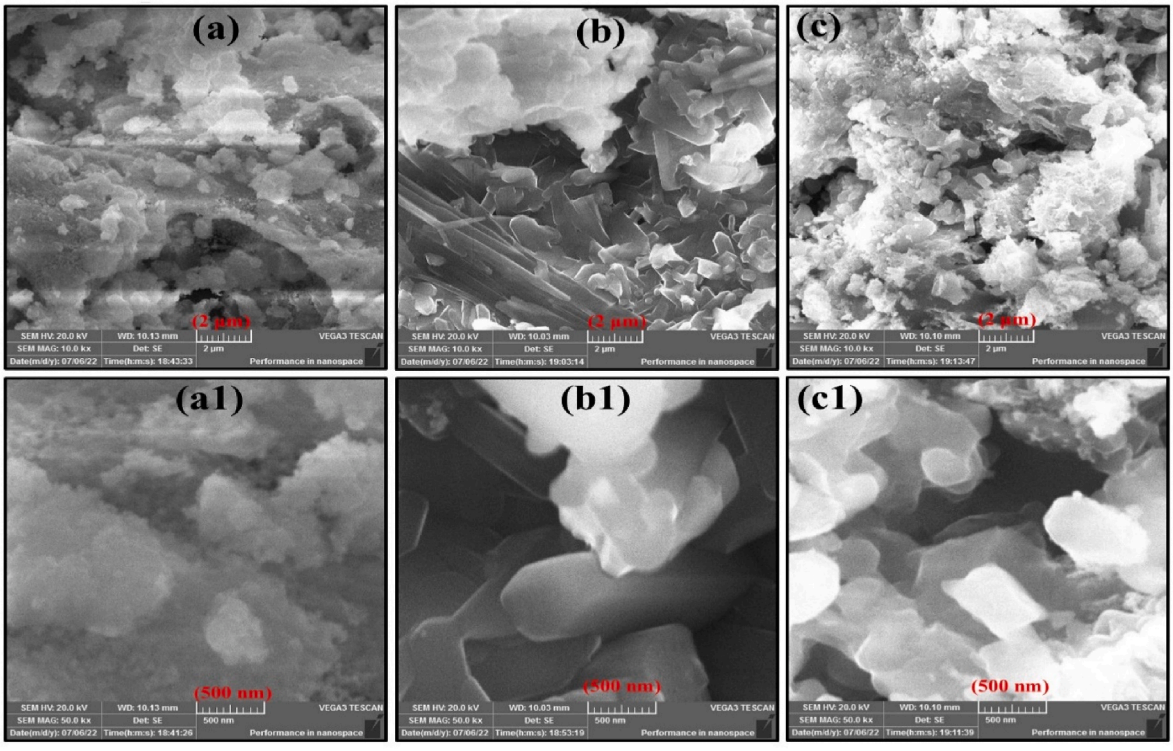

Fig. 5. SEM images of (a,a1) CeO_2 and Mn_2O_3 as N1, (b,b1) Co_3O_4 and NiO composite as N2 and (c,c1) Mn_2O_3, CeO_2, Co_3O_4 and NiO and Mn_5O_8 as multimetal oxide composite as N3.

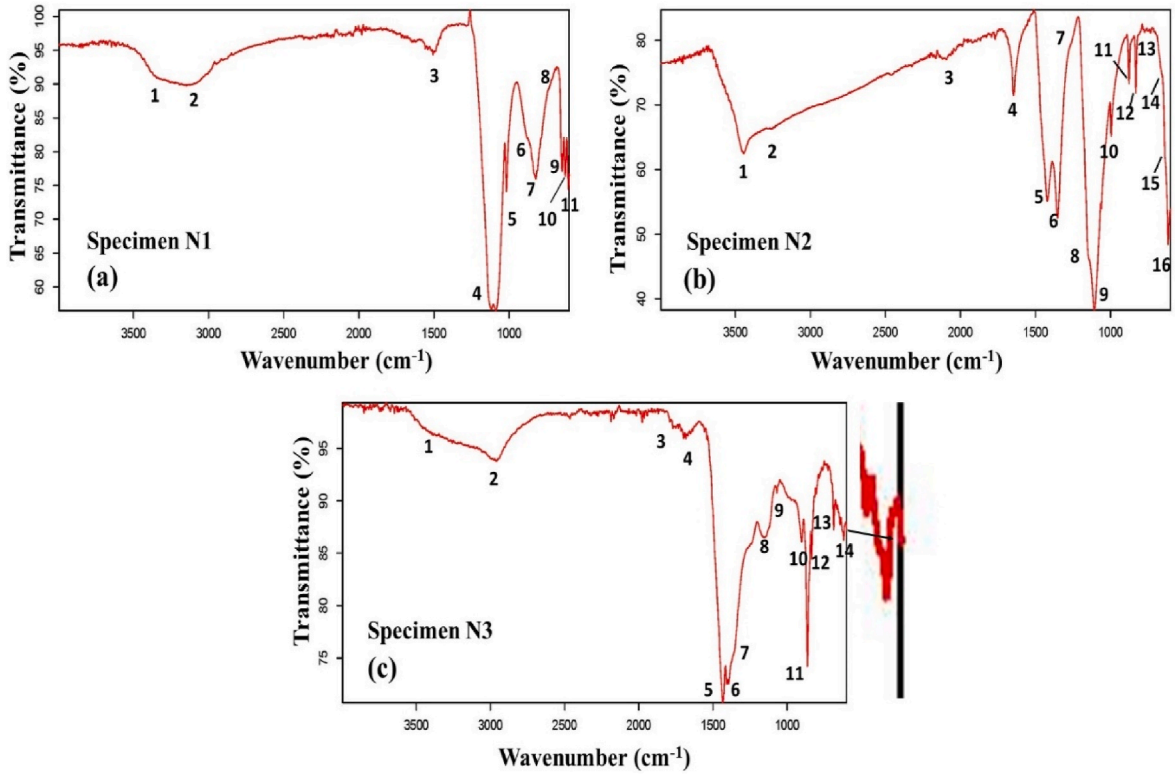

Fig. 6. FTIR spectra of composite (a) N1, (b) N2, and (c) N3.

its relatively low surface area, N2 exhibits superior electrochemical performance, likely due to its enhanced conductivity [53].

The Raman spectrum of the CeO_2 composite (N1) is shown in Fig. 3a. A broad peak at 464 cm^{-1} corresponds to the symmetric stretching of O–Ce–O, denoted by the F2g mode. This peak is associated with the stretching oscillations of O^{2-} ions surrounding Ce^{4+} ions within an octahedral CeO8 structure. A faint peak around 614 cm^{-1} is also observed, which is associated with CeO_2. The broadening of the Raman peak at 464 cm^{-1} is attributed to oxygen vacancies, which produce surplus electrons that are collected by the voids, thereby varying the oxidation state of Ce from 4+ to 3+ [54]. In the case of Mn_2O_3, the primary vibrational modes are generated from MnO_6 octahedra within the manganese oxide structure. Of the six normal vibrational modes, denoted by $\nu1$, $\nu2$, $\nu3$, $\nu4$, $\nu5$, and $\nu6$, some become active due to the layered tunnel MnO_6 octahedral structure [55]. The vibrational modes $\nu3$ and $\nu5$ at 310 and 707 cm^{-1}, respectively, are attributed to α-Mn_2O_3. Additional Raman absorptions at 122, 195, 383, 488, 563, 621, and 655 cm^{-1} are characteristic of Mn_2O_3 [49].

The Raman spectrum depicted in Fig. 3b reveals two phases of Ni–O and one phase of Co_3O_4. The Raman peaks of NiO, associated with first-order scattering, are observed at 191 and 508 cm-1, while the peak at 701 cm^{-1} corresponds to second-order scattering. The slight shifting of these peaks is due to the presence of defects and non-uniform oxygen distribution, which lead to a faulty NiO structure [56,57]. As mentioned in the literature [38], the Ni_2O_3 phase crystallizes during sintering at 700 °C, with its prominent Raman peak at 628 cm^{-1} corresponding to the NiOOH phase [58]. Similarly, the characteristic Raman peaks of Co_3O_4 are marked in Fig. 3b, with peaks at 185, 468, 505, 598, 659, and 749 cm^{-1} attributed to its vibrational modes [59].

In specimen N3, the Raman spectrum also reveals the presence of an additional Mn_5O_8 phase, as shown in Fig. 3c. The peaks associated with the vibrational bands of Mn_5O_8 are identified at 173, 269, 294, 396, 480, 543, and 611 cm^{-1} [60]. The other features of the spectrum are similar to those presented in Fig. 3a–b.

The UV–Vis diffused reflectance spectra are shown in Fig. 4a. The calculated band gap energies, as depicted in Fig. 4b–d, provide crucial information about the electronic transitions in the materials. In Fig. 4b, the band gap energies for CeO_2 and Mn_2O_3 are determined to be 3.27 eV and 1.38 eV, respectively. For specimen N2, the band gap energies for Co_3O_4 and NiO are found to be 1.53 eV and 3.73 eV, respectively. In the case of specimen N3, the presence of a mixture of Mn, Ce, Ni, and Co-based oxides is confirmed through their respective band gap energies. Specifically, in the literature, the band gap energy for CeO_2 is 3.43 eV [61], Mn_2O_3 is 1.43 eV, Co_3O_4 is 1.57 eV [62], NiO is 3.72 eV [63] and Mn_5O_8 is 2.54 eV. The band gap energy for CeO_2 is known to vary widely, ranging from 2.6 to 3.4 eV [64]. Therefore, the band gap energies obtained from the two independent specimens, N1 and N2, are consistent with this range. The band gap energy variations observed across different specimens is not only consistent with reported literature values but also points to the tenability of these materials for specific applications [64]. The results justify the calculated band gaps for the independent specimens, as they fall within the expected range, confirming the reproducibility and reliability of the synthesis process. This discussion emphasizes the importance of understanding band gap energies in the context of material design and application, particularly in fields like supercapacitors.

Scanning electron microscopy (SEM) images of CeO_2 and Mn_2O_3, as depicted in Fig. 5a–a1, reveal an agglomerated morphology with particles of size smaller than 100 nm with visible porous channels and voids. The small particle size and the presence of porous structures are advantageous for supercapacitor applications as they can provide a higher surface area critical for enhancing electrochemical performance by facilitating better charge storage and faster ion diffusion. The SEM images of the Co_3O_4, NiO, and Ni_2O_3 composite, shown in Fig. 5b, illustrate connected or merged NiO cubical columns. Additionally, the edges of these columns are not sharp, as highlighted in Fig. 5b1, with the approximate dimensions of the faces around 400 nm. The formation of cubical columns in NiO is particularly beneficial for a supercapacitor because it can improve electrical conductivity and mechanical stability, thereby enhancing the overall durability and performance. In contrast,

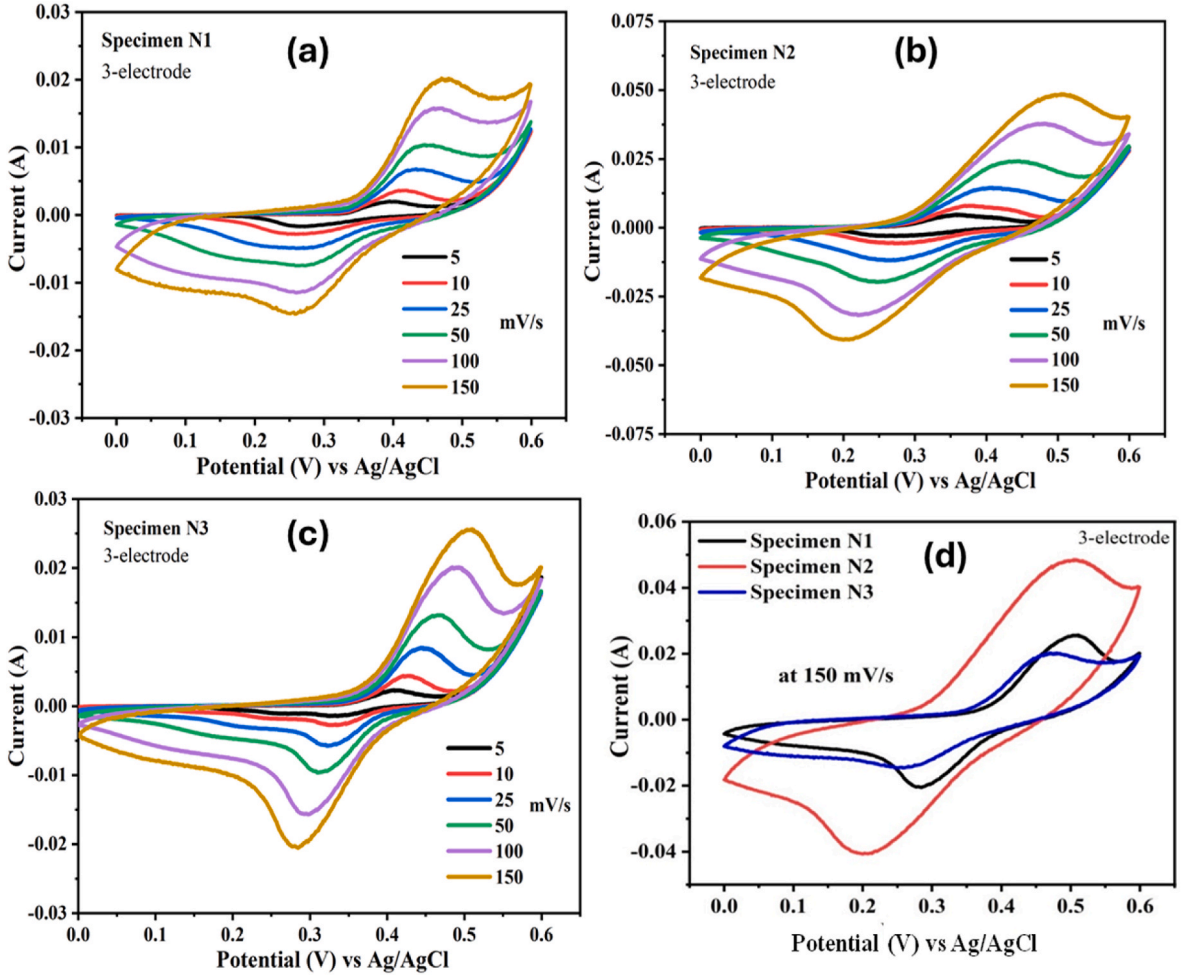

Fig. 7. For 3-electrode configuration, CV curves of specimens N1 (a), N2 (b), and N3 (c). Comparison of CV curves at 150 mV/s (d).

Co_3O_4 appears as rectangular plates within the merged NiO structure with varying sizes below 100 nm. The mixed morphology of all four metal oxides developed during synthesis is presented in Fig. 5c–c1, where all phases coexist in relatively large particles, manifesting as cubical, spherical, and plateau-like forms. This diverse morphology can potentially lead to a synergistic effect, combining the high capacitance of the transition metal oxides with the structural stability provided by the different morphologies. Such a combination is desirable in supercapacitors as it can result in improved charge/discharge rates, higher energy density, and prolonged cycle life.

To examine the characteristic bonds in the prepared specimens N1, N2, and N3, their respective FTIR spectra are presented in Fig. 6a–c. The FTIR spectra reveal absorption peaks (as numbered in Fig. 6a–c that indicate the features of the prepared materials. In the case of composite N1 (Fig. 6a), the transmittance peaks between 3000 and 3500 cm^{-1} are attributed to O–H stretching vibrations associated with the common hydroxyl group. At 1025 cm^{-1}, there is a synergistic vibration mode of Mn with the hydroxyl group, which suggests a strong interaction between Mn and oxygen, potentially enhancing redox activity—a desirable property for high-capacitance materials. Additionally, stretching vibrations at 628 and 522 cm^{-1} are associated with the tetrahedral and octahedral sites in Mn–O bonds [65,66]. CeO_2, another component of the composite N1, exhibits stretching vibrations (Ce–O) at 500 and 525 cm^{-1} [67]. CeO_2 is known for its high oxygen storage capacity and fast oxygen transport, which can enhance the charge-discharge rates in supercapacitors. The strong absorption peak at 1114 cm^{-1} is due to the Ce–OH band [68], and the peak at 845 cm^{-1} corresponds to O–C–O stretching vibrations [69], which may arise from surface-adsorbed carbonate species, possibly contributing to pseudocapacitive behavior.

FTIR spectrum of composite N2, shown in Fig. 6b, includes Ni–O and Co–O phases. Stretching modes related to the hydroxyl group (-OH) are present in the range 3300–3500 cm^{-1}, and a hydroxyl band at 1655 cm^{-1} represents the bending mode of water. The absorption peak at 841 cm^{-1} is attributed to Co–O rocking vibrations [70,71]. Peaks at 561 and 669 cm^{-1} indicate the presence of Co_3O_4 [72]. Although the fundamental stretching band of Ni–O (around 450 cm^{-1}) is beyond the detection limit of the FTIR measurements, it is confirmed by XRD results. Additionally, peaks at 1375, 997, and 1437 cm^{-1} are associated with –OH groups in Ni–O, validating the formation of NiO particles during post-synthesis sintering [73]. NiO is a widely used material in supercapacitors due to its high specific capacitance and good cycling stability. Peaks in the 500–1000 cm^{-1} range are attributed to C–O-based modes [74].

FTIR spectrum of composite N3 as a combination of Mn–O, Ce–O, Ni–O, and Co–O phases, is shown in Fig. 6c. Characteristic bands are evident in all composites. For instance, the absorption peak at 500 cm^{-1} is associated with the stretching mode of CeO_2 [67], the peak at 520 cm^{-1} is attributed to the Mn–O stretching mode [66], and the absorption peak at 841 cm^{-1} corresponds to Co–O rocking vibrations [70]. The presence of Ni–O is indicated by a –OH bond with nickel oxide at 1421 cm^{-1}, suggesting that the material might exhibit good electrochemical performance due to the combination of high conductivity and redox activity of NiO. The integration of these various metal oxides within composite N3 suggests a synergistic effect, potentially leading to improved electrochemical performance, higher energy density, and better cycling stability, which will be discussed in the next section.

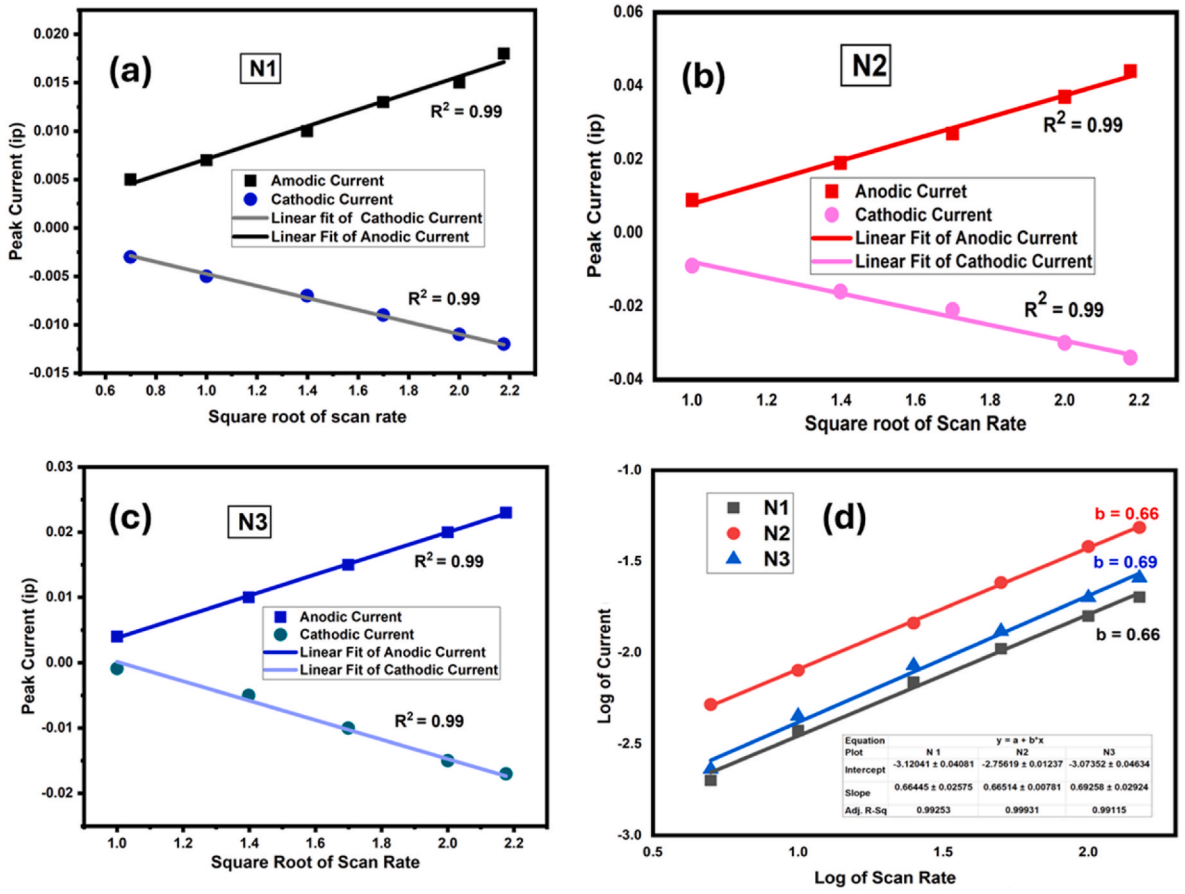

Fig. 8. (a) R^2 value of N1, (b) N2, and (c) N3. (d) The b-value is a slope of the logarithmic plot between the peak current and scan rate for N1, N2, and N3.

The cyclic voltammograms (CVs) of all the prepared electrode materials are shown in Fig. 7a–c and exhibit both reduction and oxidation peaks. For all materials, the pseudocapacitive nature is a synergistic effect of the electrochemical properties of the constituent metal oxides [20]. Redox peaks in CV profiles signify the specific redox couple and each peak is attributed to a certain oxidation and reduction process. Furthermore, the peak current, shape, and position of redox peaks provide rich information about the kinetics and thermodynamics of the processes. The area under the redox peaks is linked with electroactive species quantitatively, whereas kinetic parameters such as the rate constant for electron transfer are associated with peak current and peak potential. The position of the peak offers crucial information regarding the stability and reactivity of the species, as shifting in peak potential corresponds to the reactivity of the species with other species in the environment [2]. Notably, according to Fig. 7d, the CV loop area for N2 is larger at the same scan rate as N1 and N3, suggesting superior pseudocapacitive behavior. The larger loop area corresponds to a higher charge storage capability, making N2 a promising candidate for supercapacitor electrode. The presence of redox peaks suggestelectrolyte ion diffusion within the prepared composite materials (N1, N2, or N3), [75]. This pseudocapacitive nature of N2 is responsible for enhancing both energy and power densities. Moreover, the non-symmetric nature of the CV curves, which becomes more pronounced with increasing scan rates, as illustrated in Fig. 7, is likely due to the kinetic limitations of ion transport at higher scan rates. This observation implies that while these materials can store significant amounts of charge, their rate capability might be influenced by the ion diffusion dynamics within the electrode matrix [76]. A comparative analysis of the CVs for all three samples at 150 mV/s, as presented in Fig. 7d, further underscores the superior electrochemical performance of N2, which could be attributed to its optimized composition and microstructure, making it particularly suitable for high-performance supercapacitor applications.

The value of R^2 for the CV graph is a critical parameter in assessing the reversibility of the redox process. A value of R^2 close to 1 indicates a reversible reaction, which is desirable in electrochemical systems where efficiency and stability are paramount [77]. To determine the R^2 value, the peak currents are plotted as a function of the square root of the scan rates. In this study, the R^2 values for N1, N2, and N3 are 0.99, as shown in Fig. 8a–c. To investigate the diffusion-based processes and surface-controlled mechanisms of charge storage in the current composite materials, equations (2) and (3) are used to calculate the b-value, which reveals the nature of the charge storage processes [78].

$$i = av^b \tag{2}$$

$$\log(i) = \log(a) + b \log(v) \tag{3}$$

In these equations, v represents the scan rate, i denotes the peak current, and a and b are adjustable constants. Capacitors typically exhibit a b-value between 0.8 and 1, while battery-like materials have b-valuer-anging from 0 to 0.5. Pseudocapacitors, however, possess b-value ranging from 0.5 to 0.8, reflecting a hybrid mechanism involving both surface-controlled and diffusion-limited processes. The b-values for all

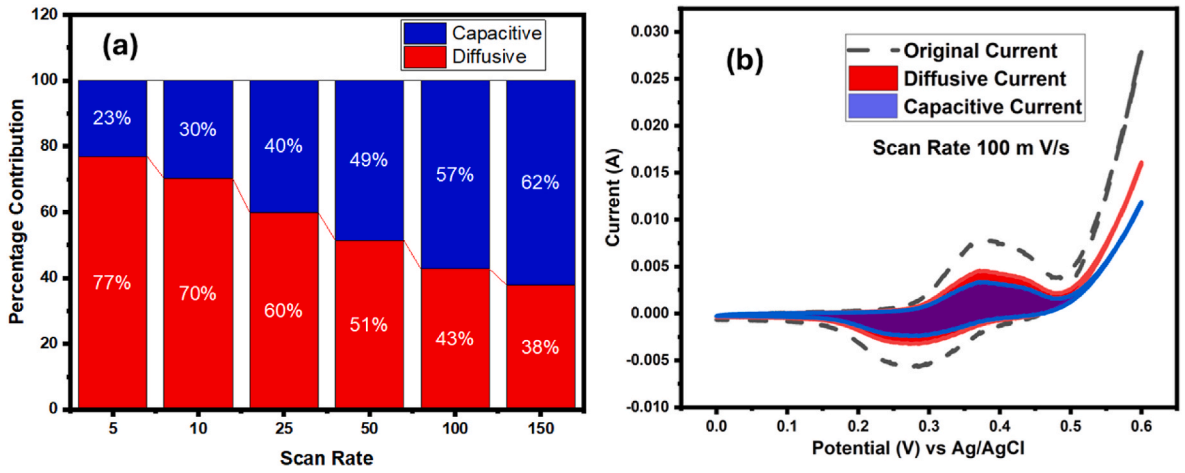

Fig. 9. (a) Percentage capacitive and diffusive contributions, a bar chart, for specimen N2 with different scan rates. (b) Diffusive and capacitive contributions for specimen N2 at the scan rate of 100 mV/s.

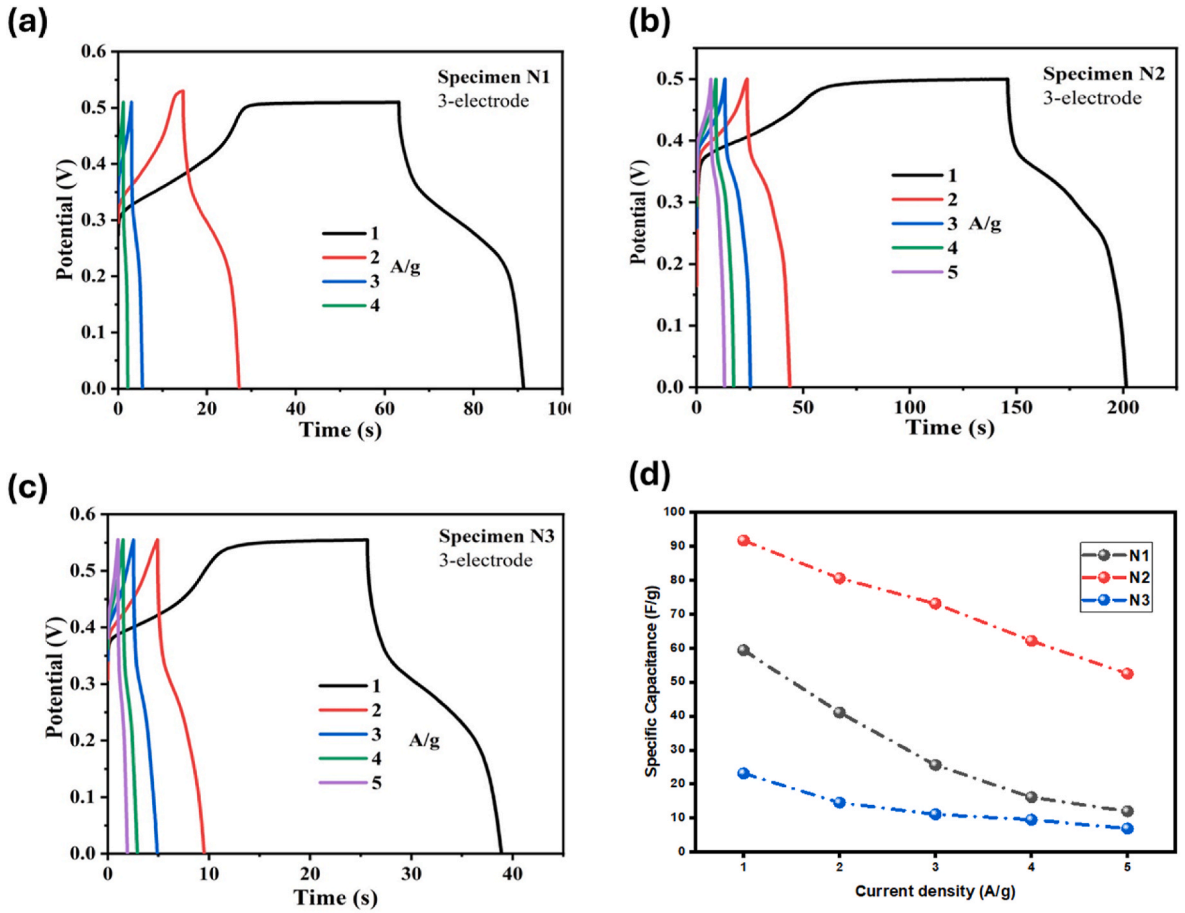

Fig. 10. For 3-electrode configuration, GCD measurements of specimens (a) N1 (b) N2 (c) N3 (d) specific capacitance as a function of current density.

materials (N1, N2, and N3) are determined by plotting the logarithm of peak current against the logarithm of scan rates (Fig. 8d), providing a clear explanation of the charge storage mechanism. The b-value for N2 is 0.69, while the b-values for both N1 and N3 are 0.66, confirming the pseudocapacitive nature of the synthesized materials. N2 may have a higher contribution from surface-controlled processes, which could be attributed to differences in material structure or morphology. This analysis highlights the effectiveness of these composite materials in supercapacitor applications, where a balance between high power density (surface-controlled) and high energy density (diffusion-limited) is critical. The near-reversible redox behavior, combined with the intermediate b-values, suggests that these materials can provide efficient energy storage and release.

To distinguish between diffusive and capacitive kinetic mechanisms in supercapacitors, Dunn's method is applied using equation (4) [79]:

$$i(V) = k_1 v + k_2 v^{1/2} \quad (4)$$

Fast surface capacitive effects are represented by $k_1 v$, diffusion-

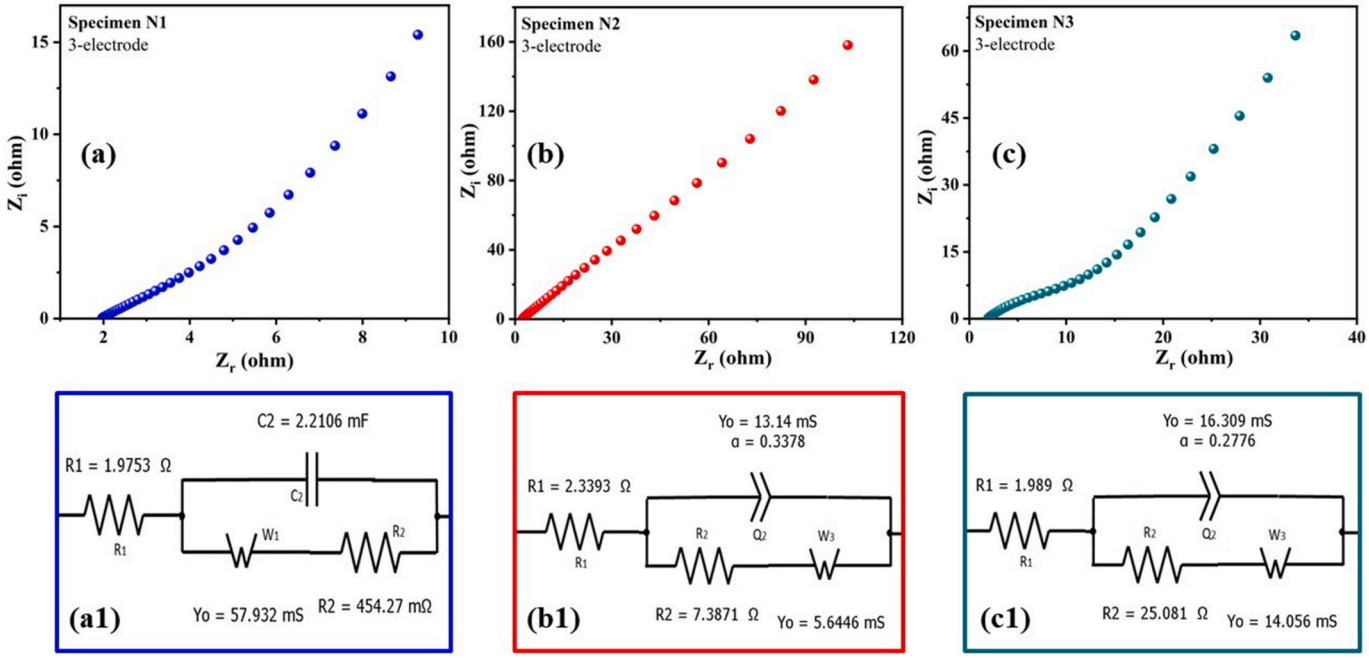

Fig. 11. EIS graphs of specimens N1 (a), N2 (b), and N3 (c) with their respective Randles circuits (a1), (b2), and (c3).

controlled reactions by $k_2v^{1/2}$, peak current by i, and scan rate by v. Plotting $i/v^{1/2}$ against $v^{1/2}$ suffices the numerical values of k_1 and k_2 parameters defined as the slope and the intercept, respectively. For the N2, the contribution of diffusion-controlled reactions is calculated as 77% at a scan rate of 5 mV/s. This contribution decreases to 38% as the scan rate increases to 150 mV/s. Conversely, the capacitive contribution rises from 23% to 62% over the same range of scan rates, as illustrated in Fig. 9a. These results highlight the increasing dominance of capacitive behavior at higher scan rates, which is typical for supercapacitor materials as the charging process becomes more surface-oriented with faster scanning.

Additionally, the CV spectrum of N2 at a scan rate of 100 mV/s is shown in Fig. 9B. The total current (represented by the dashed black line) is decomposed into its diffusive (red line) and capacitive (blue line) components, demonstrating the distinct contributions of each mechanism at this particular scan rate. This analysis underscores the dual nature of charge storage in electrode material, where both surface adsorption and diffusion-controlled processes play critical roles depending on the operational conditions.

The GCD curves exhibit a non-linear trend with asymmetric charging and discharging behavior for all samples (N1, N2, and N3), indicating quasi-reversible faradaic reactions [79], as illustrated in Fig. 10a–c. This behavior suggests that during faradaic reactions, the charge-to-voltage ratio is not uniform over time. Such non-linearity and asymmetry are characteristic of supercapacitors where pseudocapacitive behavior dominates, as opposed to purely electrostatic double-layer capacitance. This pseudocapacitance arises from redox reactions, intercalation processes, or electrosorption that occurs at the electrode-electrolyte interface, which leads to the observed quasi-reversible faradaic reactions. Consequently, the specific capacitance is calculated using equation (5) [80]:

$$C_s = \frac{2 \times i \times \int V dt}{m \times V^2} \quad (5)$$

where i is the current supplied to the electrode, $\int Vdt$ is the area under the discharging curve, m is the mass of active materials, and V is the potential window involved in the discharging process. This equation is essential as it accounts for the non-linear charge-discharge behavior, ensuring that the calculated capacitance accurately reflects the performance under real operational conditions. Using equation (5), the specific capacitances are plotted against current density, as shown in Fig. 10d. The maximum specific capacitances obtained from the GCD analysis at 1 A/g are 59.3, 91.67, and 23.14 F/g for N1, N2, and N3, respectively. These values highlight the effectiveness of the electrode materials and their architecture in enhancing charge storage capability. Notably, sample N2 demonstrates the highest specific capacitance, suggesting superior electrochemical activity.

Table 1
Series and charge transfer resistances after model fitting of the Nyquist plots of N1, N2, and N3.

Specimen	R_s (ohm)	R_{CT} (ohm)	W (S)
N1	1.98	0.454	0.058
N2	2.34	7.39	0.056
N3	1.99	25.08	0.014

The EIS results (Fig. 11) provide crucial insights into the performance of the composite electrode materials, alongside their corresponding equivalent circuits. The key electrochemical impedance parameters include series resistance (R_s), charge transfer resistance (R_{ct}), and Warburg conductance (W) which are summarized in Table 1. The 45° inclination of the Nyquist plot's straight line in the low-frequency region indicates mass transfer [81]. This diffusion behavior suggests that ion transport within the electrode materials is not purely capacitive but involves a resistive component due to ion diffusion through the electrode's porous structure. The Warburg impedance typically arises from the interaction between ions and the electrode surface, highlighting the importance of optimizing material properties for efficient charge storage. The observed diffusion-based mechanism is intimately linked to the surface characteristics of the electrodes, which are determined by the morphology, grain structure, and the presence of inter- and intra-grain boundaries. Specifically, these factors critically influence electrochemical behavior in the multimetal oxide-based composite systems N1, N2, and N3.

The superior specific capacitance exhibited by the N2 (Ni–O/Co_3O_4) material highlights its potential as a high-performance electrode for supercapacitors. Constructing a hybrid supercapacitor using N2 as the cathode and activated carbon (AC) as the anode allows for integrating

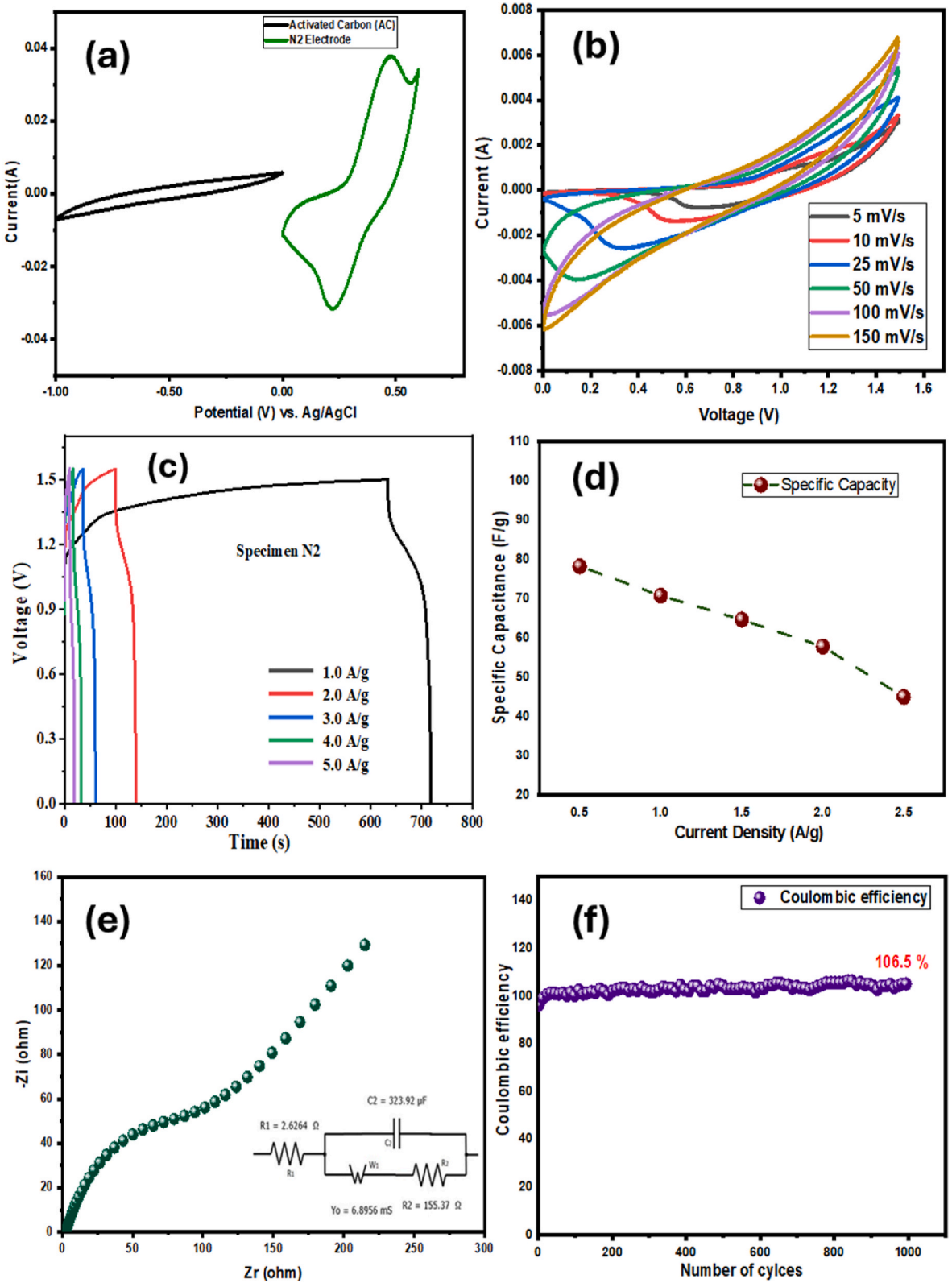

Fig. 12. For two-electrode assembly. (a) CV curves of specimens N2 and activated carbon. (b) CV curves of the hybrid device at different scan rates. (c) GCD curves of hybrid devices at different current densities. (d) Specific capacitance as a function of current density and (e) EIS graph and (f) Cyclic stability/Coulombic efficiency of the hybrid device after 1000 GCD cycles.

Table 2
Variation of specific energy and specific power with changing current density for two-electrode assembly.

Current Density (A/g)	Current Density (A/g)	Specific Power P_s (W/kg)
1	24.45	1086.80
2	22.19	1996.87
3	19.69	2625.00
4	18.44	4148.44
5	16.19	5271.88

both faradaic and non-faradaic energy storage mechanisms, offering enhanced energy and power density. The CVs shown in Fig. 12a demonstrate the distinct electrochemical behavior of each electrode within the potential window of 0 V–1.5 V. The AC electrode, operating in the potential range of 0 V to −1.0 V, exhibits classic capacitive behavior characterized by electrostatic adsorption at the electrode-electrolyte interface, typical for electric double-layer capacitors (EDLCs). On the other hand, the N2 electrode, in the range of 0 V–0.5 V, displays pseudocapacitive behavior due to reversible faradaic redox reactions, which is a hallmark of transition metal oxide-based electrodes. The performance of the hybrid supercapacitor, evaluated through CV measurements at various scan rates (Fig. 12b), reveals the dynamic response of the device. The quasi-rectangular shape of the CV curves at higher scan rates, although deviating from the ideal rectangular form, underscores the limitations in ion transport on the electrode surface during rapid redox processes. This behavior is typical in hybrid supercapacitors, where the combination of capacitive and pseudocapacitive processes introduces complexity in the charge-discharge dynamics, particularly at high scan rates where ion diffusion becomes a limiting factor.

GCD curves in Fig. 12c further corroborate the dual nature of the hybrid device. The observed decrease in specific capacitance from 78.25 F/g at 1 A/g to 44.95 F/g at 5 A/g (Fig. 12d) is indicative of the rate-dependent performance often seen in hybrid systems. GCD profiles of three-electrode and two-electrode show variation at lower current density, which is attributed to the different electrode interactions and charge distribution. A reference electrode in a three-electrode set-up provides considerable control on measurements by providing stable potential and a counter electrode helps in balancing charge distribution effectively to prevent resistive losses. In two-electrode assembly, significant resistive losses are observed, which affect the performance of practical devices. Moreover, at a lower current density, there is a uniform current flow in a three-electrode setup, whereas concentration polarization or localized heating may be experienced in a two-electrode assembly. Different electrode environments are also responsible for the kinetics of electrochemical reactions, as the three-electrode system may enable faster reaction rates as compared to the two-electrode assembly, showing different GCD profiles. As the current density increases, the reduced time for ion diffusion and charge transfer leads to a lower accessible surface area, thereby decreasing the specific capacitance. This trade-off between energy and power density is a critical consideration in the design of hybrid supercapacitors. The specific energy (Es) and specific power (Ps) for the two-electrode cell are calculated using equations (6) and (7) [82]:

$$E_s = \frac{i \times \int V dt}{3.6 \times m} \tag{6}$$

$$P_s = \frac{Es \times 3.6}{td} \tag{7}$$

The calculated Es and Ps values of 24.45 Wh/kg and 1086.8 W/kg, respectively, at 1 A/g (Table 2), illustrate the balanced performance of the hybrid supercapacitor. These metrics are essential in determining the practical applicability of the device in real-world applications, where both high energy and power densities are desired.

EIS analysis, as shown in Fig. 12e, reveals a low R_s of 2.62 Ω, indicative of efficient ion transport and minimal internal resistance within the device. The charge R_{ct} of 155.37 Ω, represented by the semicircle in the Nyquist plot, provides insight into the kinetics of the redox processes at the electrode interface. The vertical line at lower frequencies further suggests efficient mass transport, with the diffusion of hydroxyl ions being the rate-limiting step. The exceptional cyclic stability of the hybrid device, with a coulombic efficiency of 106.5% over 1000 GCD cycles (Fig. 12f), features its long-term durability and potential for practical applications. This high coulombic efficiency, coupled with the robust electrochemical performance, makes the N2-based hybrid supercapacitor a promising candidate for energy storage systems where both high power and energy densities are required.

Present results are compared with recent studies over similar electrode materials in Table 3.

4. Conclusion

Employing a facile and cost-effective solution combustion method, we have successfully synthesized three different composites (N1, N2, and N3) of mixed metal oxides based on Ce, Mn, Ni, and Co metals. These composites are characterized in terms of their structural, optical, and morphological properties. The existence of CeO_2, Mn_2O_3, Co_3O_4, NiO, Ni_2O_3, and Mn_5O_8 phases has been identified by XRD. Molecular dynamics has been studied by Raman and FTIR spectra in terms of characteristic vibrational modes. Due to the different chemical natures of metal oxide-based phases, they have been crystallized as columns and in irregular shapes. The exhibited particles agglomerated together give rise to porous channels and voids critical for the charge storing purposes. The average pore dimensions of 93.4037 Å have been measured for the Co_3O_4/Ni–O composite with a surface area of 2.0772 m^2/g. Electrochemical measurements have been conducted using two-electrode and three-electrode configurations to estimate their potential as electrode materials. The pseudocapacitive nature has been found for all samples. Among the composites, multiphase Ni–O/Co_3O_4 (N2) is a better electrode material, and the electrochemical findings have been correlated with other characterization results. The other composites, as electrode material, have a specific capacitance of 59.3 and 23.14 F/g at 1A/g for N1 and N3, respectively. Notably, the N2 composite demonstrates superior capacitive performance, achieving a specific capacitance of 91.67 F/g at a current density of 1 A/g. To assess its practical application, a device is fabricated using N2 as cathode against an activated carbon anode, resulting in a specific capacitance of 78.25 F/g, specific energy of 24.45 Wh/kg, and specific power of 1086.80 W/kg at 1 A/g, along with a coulombic efficiency of 106.5% over 1000 GCD cycles. The underlying diffusion-capacitive controlled process highlights the synthesized material's potential as a promising candidate for hybrid energy storage devices.

CRediT authorship contribution statement

Nayab Zahra: Writing – original draft. **Muhammad Shahbaz:** Writing – original draft. **Mohsin Saleem:** Writing – original draft, Supervision, Methodology, Investigation, Formal analysis. **Muhammad Zubair Khan:** Writing – original draft. **Muneeb Irshad:** Writing – original draft. **Shahzad Sharif:** Writing – original draft. **Jung Hyuk Koh:** Writing – original draft. **Mohsin Ali Marwat:** Writing – original draft. **Gwangseop Lee:** Writing – original draft. **Muhammad Irfan:** Writing – original draft. **Abdul Ghaffar:** Writing – original draft, Supervision, Methodology, Investigation, Formal analysis, Conceptualization.

Declaration of competing interest

The authors declare that they have no known competing financial interests or personal relationships that could have appeared to influence the work reported in this paper.

Table 3
Comparison of properties with other work.

Ref.	Method	Heat treatment	Electrode material	Morphology	Crystallite size (nm)	Particle size (nm)	Electrolyte	Sp. capacitance (F/g)	At rate	Retention (%)	Power density (W/kg)	Energy density (Wh/kg)
This work	Solution combustion	700 °C	Combinations of Mn–O, CeO_2, Ni–O, Co_3O_4	Cubical columns	–	–	1 M KOH	78.25	1 A/g	106@1000 gcd cycles	1086.80	24.45
[83]	Chemical precipitatioion	300 °C	MnO_2/rGO	Nanoflakes	–		1 M Na_2SO_4	140.3	1 mA	99.4@10000 gcd cycles	633.7	19.5
[84]	Hydrothermal	120 °C and 60 °C	CeO_2–MnO_2-rGO	Granular-honeycomb-nanosheets	–	40–50	–	466	1 A/g	100@10000 gcd cycles	1008	259
[33]	Hydrothermal	120 °C and 300 °C	MnO_2–CeO_2-	Spherical, ellipsoidal, rod-like, agglomeration	–	–	3 mol L^{-1} KOH	274.3	0.5 A/g	93.9@1000 gcd cycles	–	34.29
[85]	Hydrothermal	120 °C and 500 °C	NiO/Co_3O_4/rGO	Nanoparticles	–	20–40	3 M KOH	980	1 A/g	92@5000 gcd cycles@10 A/g	1396.3	23.7
[79]	Coprecipitation	100 °C and 500 °C	Co_3O_4/NiO	Agglomerated semi-spherical nanoparticles	21–25	–	2 M KOH	2769.2	0.005 V/s	96.2@ 2500 gcd cycles	3629.76@7 A/g	131.96 @ 1 A/g
[86]	Chemical synthesis	550 °C	$Ag_2Mo_2O_7$	Nanoflake	11.19	–	1 M KOH	430 C/g	1 A/g	93.7%@ 5000 gcd cycles	–	–
[87]	One-step calcination	400 °C	C/NiO/Co_3O_4	Cubes	–	500	6 M KOH	208.5	1 A/g	87.1@5000 cycles	750	32.6
[88]	Hydrothermal	500 °C	NiO–CoO	Spherical	40 (NiO) 49 (CoO)	–	1.1 g KOH	298	0.01 V/s	94.3@5000 gcd cycles	–	–
[89]	Chemical method	400 °C	$Zn_3V_2O_8$	Nanosphere	36	–	1 M KOH	471	1 A/cm^2	97@3000 cycles	–	–
[90]	Hydrothermal (solvent-mediated synthesis)	500 °C	Co_3O_4/CeO_2	Porous dendritic	–	10 nm (branches)	6 M KOH	276.3	0.5 A/g	91.2@2000 gcd cycles	400	10.5
[91]	Co-precipitation	80 °C and 60 °C	MnO_2/CoO	Agglomerated particles	–	132.86 nm (MnO_2) 157.87 nm (CoO)	Pedot: PSS & cellulose paper	44.92	0.025 V/s	~70	5.62 W/g	22.46 J/g
[92]	Wet chemical route	500 °C	$SrMoO_4$	Stone like structure	42.7	–	1 M KOH	384 C/g	0.005 V/s	91.1@ 5000 gcd at 1 A/g	3150	67.3
[93]	Hydrothermal	550 °C	CeO_2/NiO	Cauliflower's leaf-like	8–10	–	3 M KOH	8.418	0.0001 A/g	–	0.025	1.052
[94]	Hydrothermal	500 °C	NiO/MnO_2/rGO	Cubic	32.18	80	3 M KOH	536	1 A/g	93@3000 cycles	–	–
[95]	Wet chemical method	500 °C	ZrV_2O_7	Stone-like particles	–	–	1 M KOH	679	5 mV/s	92.5%@ 3000 gcd cycles	–	–

Acknowledgment

This work was jointly supported by the National Research Program of Universities (NRPU), the Higher Education Commission, (HEC), Pakistan research fund "Development of lab/pilot scale facilities for the production of piezoelectric material for multilayer energy devices" 20-15673/NRPU/R&D/HEC/2021 and MSIT (Ministry of Science and ICT), Korea, under the ITRC (Information Technology Research Centre) support program (IITP-2025-RS-2020-II201655, 50%) supervised by the IITP (Institute of Information and Communications Technology Planning And Evaluation).

Data availability

Data will be made available on request.

References

[1] H. Pontzer, et al., Daily energy expenditure through the human life course, Science 373 (6556) (2021) 808–812.
[2] C.P. Grey, D.S. Hall, Prospects for lithium-ion batteries and beyond—a 2030 vision, Nat. Commun. 11 (1) (2020) 1–4.
[3] M. Ali, et al., High-entropy battery materials: revolutionizing energy storage with structural complexity and entropy-driven stabilization, Mater. Sci. Eng. R Rep. 163 (2025) 100921.
[4] M. Prajapati, et al., Recent advancement in metal-organic frameworks and composites for high-performance supercapatteries, Renew. Sustain. Energy Rev. 183 (2023) 113509.
[5] R. Srinivasan, et al., Enhanced electrochemical behaviour of Co-MOF/PANI composite electrode for supercapacitors, Inorg. Chim. Acta. 502 (2020) 119393.
[6] J. Liu, et al., Constructing high-capacitance electrochemical capacitors through the introduction of V ions into MoS2/Ni3S2 nanosheets, Materials Today Sustainability 23 (2023) 100433.
[7] S.Z. Golkhatmi, M.I. Asghar, P.D. Lund, A review on solid oxide fuel cell durability: latest progress, mechanisms, and study tools, Renew. Sustain. Energy Rev. 161 (2022) 112339.
[8] M.B. Hanif, et al., Innovative advances and challenges in solid oxide electrolysis cells: exploring surface segregation dynamics in perovskite electrodes, Mater. Sci. Eng. R Rep. 161 (2024) 100864.
[9] M.E. Şahin, F. Blaabjerg, A. Sangwongwanich, A comprehensive review on supercapacitor applications and developments, Energies 15 (3) (2022) 674.
[10] L. Zhang, et al., A review of supercapacitor modeling, estimation, and applications: a control/management perspective, Renew. Sustain. Energy Rev. 81 (2018) 1868–1878.
[11] W. Raza, et al., Recent advancements in supercapacitor technology, Nano Energy 52 (2018) 441–473.
[12] M. Kandasamy, et al., Recent advances in engineered metal oxide nanostructures for supercapacitor applications: experimental and theoretical aspects, J. Mater. Chem. A 9 (33) (2021) 17643–17700.
[13] M.S. Yadav, Metal oxides nanostructure-based electrode materials for supercapacitor application, J. Nanoparticle Res. 22 (12) (2020) 367.
[14] N. Kumar, et al., Recent advanced supercapacitor: a review of storage mechanisms, electrode materials, modification, and perspectives, Nanomaterials 12 (20) (2022) 3708.
[15] X. He, X. Zhang, A comprehensive review of supercapacitors: properties, electrodes, electrolytes and thermal management systems based on phase change materials, J. Energy Storage 56 (2022) 106023.
[16] L. Phor, A. Kumar, S. Chahal, Electrode materials for supercapacitors: a comprehensive review of advancements and performance, J. Energy Storage 84 (2024) 110698.
[17] I. Rabani, et al., The role of uniformly distributed ZnO nanoparticles on cellulose nanofibers in flexible solid state symmetric supercapacitors, J. Mater. Chem. A 9 (19) (2021) 11580–11594.
[18] C. Bathula, et al., Sonochemically exfoliated polymer-carbon nanotube interface for high performance supercapacitors, J. Colloid Interface Sci. 606 (2022) 1792–1799.
[19] C. Bathula, et al., Highly efficient solid-state synthesis of Co3O4 on multiwalled carbon nanotubes for supercapacitors, J. Alloys Compd. 887 (2021) 161307.
[20] R.R. Palem, et al., Enhanced supercapacitive behavior by CuO@MnO2/carboxymethyl cellulose composites, Ceram. Int. 47 (19) (2021) 26738–26747.
[21] S. Rajkumar, et al., Recovery of copper oxide nanoparticles from waste SIM cards for supercapacitor electrode material, J. Alloys Compd. 849 (2020) 156582.
[22] M. Anwar, et al., Solution-combustion synthesis of AgCo3O4/FeMn-O multiphase composite for high-performance asymmetric supercapacitor, J. Energy Storage 105 (2025) 114602.
[23] M.Z. Ansari, et al., Critical aspects of various techniques for synthesizing metal oxides and fabricating their composite-based supercapacitor electrodes: a review, Nanomaterials 12 (11) (2022) 1873.
[24] R. Srinivasan, et al., Electrochemical performance of l-tryptophanium picrate as an efficient electrode material for supercapacitor application, Phys. Chem. Chem. Phys. 21 (22) (2019) 11829–11838.
[25] S. Rajkumar, et al., One-pot green recovery of copper oxide nanoparticles from discarded printed circuit boards for electrode material in supercapacitor application, Resour. Conserv. Recycl. 180 (2022) 106180.
[26] C. An, et al., Metal oxide-based supercapacitors: progress and prospectives, Nanoscale Adv. 1 (12) (2019) 4644–4658.
[27] N. Parveen, et al., Manganese oxide as an effective electrode material for energy storage: a review, Environ. Chem. Lett. 20 (1) (2022) 283–309.
[28] F. Hong, et al., Significant improvement in Mn2O3 transition metal oxide electrical conductivity via high pressure, Sci. Rep. 7 (1) (2017) 44078.
[29] Y.-M. Li, et al., Review and prospect of MnO2-based composite materials for supercapacitor electrodes, Ionics 27 (2019) 3699–3714.
[30] N. Maheswari, G. Muralidharan, Supercapacitor behavior of cerium oxide nanoparticles in neutral aqueous electrolytes, Energy & Fuels 29 (12) (2015) 8246–8253.
[31] S. Arunpandiyan, et al., Decoration of CeO2 nanoparticles on hierarchically porous MnO2 nanorods and enhancement of supercapacitor performance by redox additive electrolyte, J. Alloys Compd. 861 (2021) 158456.
[32] L. Liu, J. Shi, R. Wang, Facile construction of Mn2O3@CeO2 core@shell cubes with enhanced catalytic activity toward CO oxidation, J. Solid State Chem. 269 (2019) 419–427.
[33] H. Zhang, et al., Hierarchical porous MnO2/CeO2 with high performance for supercapacitor electrodes, Chem. Eng. J. 286 (2016) 139–149.
[34] X. Hu, et al., Reviews and prospectives of Co3O4-based nanomaterials for supercapacitor application, ChemistrySelect 5 (17) (2020) 5268–5288.
[35] F.I. Dar, K.R. Moonoosawmy, M. Es-Souni, Morphology and property control of NiO nanostructures for supercapacitor applications, Nanoscale Res. Lett. 8 (1) (2013) 363.
[36] S. Vijayakumar, S. Nagamuthu, G. Muralidharan, Supercapacitor studies on NiO nanoflakes synthesized through a microwave route, ACS Appl. Mater. Interfaces 5 (6) (2013) 2188–2196.
[37] S.D. Dhas, et al., Synthesis of NiO nanoparticles for supercapacitor application as an efficient electrode material, Vacuum 181 (2020) 109646.
[38] S. Chen, et al., Rational design and synthesis of NixCo3−xO4 nanoparticles derived from multivariate MOF-74 for supercapacitors, J. Mater. Chem. A 3 (40) (2015) 20145–20152.
[39] F. Khalid, et al., Improved super capacitive performance of hydrothermally developed Mn and Ni oxides along with activated carbon as ternary nanocomposite, J. Phys. Chem. Solid. 161 (2022) 110467.
[40] Y. Wang, et al., Wireless multiferroic memristor with coupled giant impedance and artificial synapse application, Advanced Electronic Materials 8 (10) (2022) 2200370.
[41] M.B. Askari, et al., NiO-Co3O4-rGO as an efficient electrode material for supercapacitors and direct alcoholic fuel cells, Adv. Mater. Interfac. 8 (15) (2021) 2100149.
[42] M. Haseeb, et al., Effect of sintering temperature on microstructure, optical and dielectric properties in a low radio frequency range of a BaO:ZnO composite, Ceram. Int. 49 (21) (2023) 33445–33458.
[43] S.T. Aruna, A.S. Mukasyan, Combustion synthesis and nanomaterials, Curr. Opin. Solid State Mater. Sci. 12 (3) (2008) 44–50.
[44] A.S. Mukasyan, P. Dinka, Novel approaches to solution-combustion synthesis of nanomaterials, Int. J. Self-Propag. High-Temp. Synth. 16 (1) (2007) 23–35.
[45] S. Sharif, et al., Structural, DFT and redox activity investigation of 2D silver based MOF for energy storage devices, J. Electroanal. Chem. 961 (2024) 118226.
[46] M. Shahbaz, et al., Enhanced electrochemical performance of cerium-based metal organic frameworks derived from pyridine-2,4,6-tricarboxylic acid for energy storage devices, J. Energy Storage 88 (2024) 111463.
[47] Y. Hanifehpour, M.A. Cheney, S.W. Joo, Sonocatalytic decolorization of azo dye by ultrasound-assisted ytterbium-substituted Mn2O3 nanocatalyst, J. Inorg. Organomet. Polym. Mater. 28 (5) (2018) 2143–2153.
[48] P. Tamizhdurai, et al., Environmentally friendly synthesis of CeO2 nanoparticles for the catalytic oxidation of benzyl alcohol to benzaldehyde and selective detection of nitrite, Sci. Rep. 7 (1) (2017) 46372.
[49] H.R. Barai, et al., Synthesis of amorphous manganese oxide nanoparticles – to – crystalline nanorods through a simple wet-chemical technique using K+ ions as a 'growth director' and their morphology-controlled high performance supercapacitor applications, RSC Adv. 6 (82) (2016) 78887–78908.
[50] J. Mujtaba, et al., Nanoparticle decorated ultrathin porous nanosheets as hierarchical Co3O4 nanostructures for lithium ion battery anode materials, Sci. Rep. 6 (1) (2016) 20592.
[51] H. Qiao, et al., Preparation and characterization of NiO nanoparticles by anodic arc plasma method, J. Nanomater. 2009 (1) (2009) 795928.
[52] D.-H. Kwon, et al., Observation of the Ni2O3 phase in a NiO thin-film resistive switching system, Phys. Status Solidi Rapid Res. Lett. 11 (5) (2017) 1700048.
[53] M. Aghazadeh, Electrochemical preparation and characterization of Mn5O8 nanostructures, Journal of Nanostructures 8 (1) (2018) 67–74.
[54] G. Jayakumar, A. Albert Irudayaraj, A. Dhayal Raj, A comprehensive investigation on the properties of nanostructured cerium oxide, Opt. Quant. Electron. 51 (9) (2019) 312.
[55] K.L. McNesby, R.A. Pesce-Rodriguez, Applications of vibrational spectroscopy in the study of explosives, in: Handbook of Vibrational Spectroscopy, 2001.
[56] G. George, S. Anandhan, Synthesis and characterisation of nickel oxide nanofibre webs with alcohol sensing characteristics, RSC Adv. 4 (107) (2014) 62009–62020.
[57] P. Ravikumar, B. Kisan, A. Perumal, Enhanced room temperature ferromagnetism in antiferromagnetic NiO nanoparticles, AIP Adv. 5 (8) (2015).
[58] A. Lekatou, et al., Aqueous corrosion behaviour of Fe–Ni–B metal glasses, J. Alloys Compd. 483 (1) (2009) 514–518.

[59] A. Diallo, et al., Green synthesis of Co3O4 nanoparticles via Aspalathus linearis: physical properties, Green Chem. Lett. Rev. 8 (3–4) (2015) 30–36.
[60] C.B. Azzoni, et al., Thermal stability and structural transition of metastable Mn5O8: in situ micro-Raman study, Solid State Commun. 112 (7) (1999) 375–378.
[61] S.A. Ansari, et al., Band gap engineering of CeO2 nanostructure using an electrochemically active biofilm for visible light applications, RSC Adv. 4 (32) (2014) 16782–16791.
[62] J.J. Rushmittha, et al., Hybridization of CuFe2O4 by carbon microspheres with improved charge storage characteristics for high energy density solid-state hybrid supercapacitor, Materials Today Sustainability 28 (2024) 100950.
[63] M. Hashem, et al., Fabrication and characterization of semiconductor nickel oxide (NiO) nanoparticles manufactured using a facile thermal treatment, Results Phys. 6 (2016) 1024–1030.
[64] D. Sharma, B.R. Mehta, Nanostructured TiO2 thin films sensitized by CeO2 as an inexpensive photoanode for enhanced photoactivity of water oxidation, J. Alloys Compd. 749 (2018) 329–335.
[65] S.N. Amirtharaj, M. Mariappan, Rapid and controllable synthesis of Mn2O3 nanorods via a sonochemical method for supercapacitor electrode application, Appl. Phys. A 127 (8) (2021) 607.
[66] M.M. Motlagh, S.A. Hassanzadeh-Tabrizi, A. Saffar-Teluri, Influence of Mn2O3 content on the textural and catalytic properties of Mn2O3/Al2O3/SiO2 nanocatalyst, Ceram. Int. 40 (10, Part B) (2014) 16177–16181.
[67] M.E. Culica, et al., Cellulose acetate incorporating organically functionalized CeO2 NPs: efficient materials for UV filtering applications, Materials 13 (13) (2020) 2955.
[68] M.S. Pujar, et al., One-step synthesis and characterizations of cerium oxide nanoparticles in an ambient temperature via Co-precipitation method, in: AIP Conference Proceedings, vol. 1942, 2018, 1.
[69] H. Li, et al., Surfactant-assisted synthesis of CeO2 nanoparticles and their application in wastewater treatment, RSC Adv. 2 (32) (2012) 12413–12423.
[70] G. Tong, Y. Liu, J. Guan, In situ gas bubble-assisted one-step synthesis of polymorphic Co3O4 nanostructures with improved electrochemical performance for lithium ion batteries, J. Alloys Compd. 601 (2014) 167–174.
[71] R. Packiaraj, et al., Electrochemical investigations of magnetic Co3O4 nanoparticles as an active electrode for supercapacitor applications, J. Supercond. Nov. Magnetism 32 (8) (2019) 2427–2436.
[72] M. Ştefănescu, et al., Study on the obtaining of cobalt oxides by thermal decomposition of some complex combinations, undispersed and dispersed in SiO2 matrix, Journal of Thermal Analysis and Calorimetry 94 (2) (2008) 389–393.
[73] A.S. Adekunle, et al., Nanoparticles towards the degradation of nitrite (NO2-) and nitric oxide (NO), Int. J. Electrochem. Sci. 9 (6) (2014) 3008–3021.
[74] A. Sharma, et al., Extraction of nickel nanoparticles from electroplating waste and their application in production of bio-diesel from biowaste, International Journal of Chemical Engineering and Applications 6 (2015) 156–159.
[75] B. Akinwolemiwa, C. Peng, G.Z. Chen, Redox electrolytes in supercapacitors, J. Electrochem. Soc. 162 (5) (2015) A5054.
[76] P. Tang, et al., Understanding pseudocapacitance mechanisms by synchrotron X-ray analytical techniques, Energy & Environmental Materials 6 (4) (2023) e12619.
[77] V. Fourmond, N. Plumeré, C. Léger, Reversible catalysis, Nat. Rev. Chem 5 (5) (2021) 348–360.
[78] M. Sathiya, et al., V2O5-anchored carbon nanotubes for enhanced electrochemical energy storage, J. Am. Chem. Soc. 133 (40) (2011) 16291–16299.
[79] S.-B. Xia, et al., Robust hexagonal nut-shaped titanium(IV) MOF with porous structure for ultra-high performance lithium storage, Electrochim. Acta 296 (2019) 746–754.
[80] L.-Q. Mai, et al., Synergistic interaction between redox-active electrolyte and binder-free functionalized carbon for ultrahigh supercapacitor performance, Nat. Commun. 4 (1) (2013) 2923.
[81] K. Wang, et al., Cu2+-Induced length change of Ni-based coordination polymer nanorods and research on NiO-based hybrid pseudocapacitor electrodes, New J. Chem. 42 (12) (2018) 9876–9885.
[82] F. Shahbazi Farahani, et al., Trilayer metal–organic frameworks as multifunctional electrocatalysts for energy conversion and storage applications, J. Am. Chem. Soc. 144 (8) (2022) 3411–3428.
[83] V.M. Vimuna, et al., Simultaneous stirring and microwave assisted synthesis of nanoflakes MnO2/rGO composite electrode material for symmetric supercapacitor with enhanced electrochemical performance, Diam. Relat. Mater. 110 (2020) 108129.
[84] A. Xie, et al., Mesoporous CeO2-α-MnO2- reduced graphene oxide composite with ultra-high stability as a novel electrode material for supercapacitor, Surf. Interfaces 25 (2021) 101177.
[85] R. Kumar, et al., Enriched performance of practical device assisted asymmetric supercapacitor: NiO/Co3O4 intercalated with rGO nanocomposite electrodes, J. Energy Storage 85 (2024) 111075.
[86] S. Rajkumar, et al., One-step synthesis of nanostructured Ag2Mo2O7 with enhanced efficiency for supercapacitors, Ionics 30 (11) (2024) 7537–7549.
[87] L. Zhao, H. Zhang, B. Ma, Formation of carbon-incorporated NiO@Co3O4 nanostructures via a direct calcination method and their application as battery-type electrodes for hybrid supercapacitors, ACS Omega 8 (11) (2023) 10503–10511.
[88] M. Isacfranklin, et al., Hybrid NiO-CoO nanocomposite for high energy supercapacitor applications, Ceram. Int. 47 (6) (2021) 8486–8489.
[89] S. Rajkumar, E. Elanthamilan, J.P. Merlin, Facile synthesis of Zn3V2O8 nanostructured material and its enhanced supercapacitive performance, J. Alloys Compd. 861 (2021) 157939.
[90] H. Xie, et al., Solvent-assisted synthesis of dendritic cerium hexacyanocobaltate and derived porous dendritic Co3O4/CeO2 as supercapacitor electrode materials, CrystEngComm 23 (8) (2021) 1704–1708.
[91] A.S. Sebastian, A. Sobha, R. Sumangala, MnO2/CoO electrode for supercapacitor: synthesis and electrochemical performance, Mater. Today Proc. 55 (2022) 52–55.
[92] A. Sathiyan, et al., Electrochemical performance of SrMoO4 as electrode material for energy storage systems, J. Ind. Eng. Chem. 129 (2024) 521–530.
[93] N. Ahmad, et al., Structural, morphological, and electrochemical performance of CeO2/NiO nanocomposite for supercapacitor applications, Appl. Sci. 11 (1) (2021) 411.
[94] S. Seenivasan, et al., Electrochemical investigation of NiO@MnO2@rGO ternary nanocomposite based electrode material for high-performance supercapacitor applications, Ionics 29 (9) (2023) 3641–3652.
[95] S. Rajkumar, S. Gowri, J. Princy Merlin, Facile fabrication of ZrV2O7 nanostructures as an electrode material for supercapacitors, Inorg. Chem. Commun. 153 (2023) 110896.